Intrinsic Ultralow Lattice Thermal Conductivity in the Full-Heusler Compound Ba_2AgSb

Shao-Fei Wang,[1,2,3] Zhi-Gang Zhang,[4,5] Bao-Tian Wang,[1,2] Jun-Rong Zhang,[1,2,3,*] and Fang-Wei Wang[2,3,4,5,†]

[1] *Institute of High Energy Physics, Chinese Academy of Sciences, Beijing 100049, China*
[2] *Spallation Neutron Source Science Center (SNSSC), Dongguan 523803, China*
[3] *School of Nuclear Sciences and Technology, University of Chinese Academy of Sciences, Beijing 100049, China*
[4] *Beijing National Laboratory for Condensed Matter Physics, Institute of Physics, Chinese Academy of Sciences, Beijing 100080, China*
[5] *Songshan Lake Materials Laboratory, Dongguan 523808, China*

(Received 9 May 2021; revised 30 November 2021; accepted 7 February 2022; published 8 March 2022)

Full-Heusler thermoelectric materials have intrinsically low lattice thermal conductivity. Our first-principles calculations show that Ba_2AgSb is a semiconductor with an indirect band gap of 0.49 eV. The electronic band degeneracy and pockets near the Fermi level facilitate electron transport. The short phonon relaxation time, small group velocity (1.89 km s^{-1}), and large phonon scattering space reflect the intense phonon-phonon scattering. The large Grüneisen parameter (1.44) accounts for the strong phonon anharmonicity, thus the low lattice thermal conductivity of 0.5 W m^{-1} K^{-1} at 800 K. The isotropic figure of merit with a maximum value of 4.7 at 750 K is comparable to that of reported materials. The distribution of phonon momentum uncovers the important role of Ag in resisting thermal transport. The analysis of symmetry-based phonon-phonon scattering routes reveals the significance of symmetry on phonon scattering. The crystal structure of Ba_2AgSb can be used to regulate chemical elements to build high-performance thermoelectric materials. Our calculations provide an effective way to design thermoelectric materials, stimulating the study of full-Heusler materials.

DOI: 10.1103/PhysRevApplied.17.034023

I. INTRODUCTION

Thermoelectric materials, which transform waste heat into electricity and are widely used in refrigeration devices, have attracted extensive interest [1]. The thermoelectric conversion efficiency is described by the figure of merit $zT = S^2\sigma T/\kappa$, where σ is the electrical conductivity, S is the Seebeck coefficient, κ is the thermal conductivity, which consists of the contribution of lattice vibration κ_L and electron transportation κ_e, and T is the absolute temperature. According to this formula, materials with high electrical conductivity σ, large Seebeck coefficient S, and small thermal conductivity κ will give a remarkable thermoelectric performance [2]. Several methods [3] can be used to enhance the thermoelectric performance, such as introducing point defects [4], nanostructure [5,6], and doping [7–9]. Aside from optimizing existing materials [10], strategies to improve the thermoelectric efficiency are generally to seek materials with intrinsically low thermal conductivity. Therefore, materials with low lattice thermal conductivity have a significant impact on the development of thermoelectric materials.

Materials with strong phonon anharmonicity and intense phonon-phonon scattering usually have low lattice thermal conductivity [11]. The phonon-phonon scattering obeys the energy and momentum conservation conditions, and the crystal symmetry also places restrictions on possible phonon scattering channels [12]. Group theory provides a systematic framework for analyzing the impact of crystal symmetries on phonon-phonon scattering without calculating the complex interaction coefficient. Some researchers have proposed this concept to analyze the limitations of symmetry on phonon scattering [12,13]. Exploring symmetry-based phonon-phonon scattering can save resources and it also gives a primary crystal type for high-throughput screening.

Gold-based full-Heusler (FH) compounds with intrinsically low κ_L have drawn attention for their remarkable thermoelectric properties [14]. Sr_2AuBi has flat phonon dispersion and strong phonon anharmonicity, thus exhibiting a small κ_L and p-type zT of 2.1 at 300 K [15]. Ba_2AuX is predicted with a high thermoelectric figure of merit of 5–3 at 800 K [16]. A family of FH thermoelectric materials

*jrzhang@ihep.ac.cn
†fwwang@iphy.ac.cn

Ca_2YZ (Y = Au and Hg; Z = As, Sb, Bi, Sn, and Pb) [14,17] were produced with low thermal conductivity, which is comparable to that of the well-known materials Bi_2Ti_3. However, the analysis of symmetry-based phonon scattering in FH compounds ($Fm\bar{3}m$) is little reported. These studies stimulate us to search for low-cost FH thermoelectric materials and uncover the low thermal conductivity from the viewpoint of group theory.

In this article, the thermoelectric application of Ba_2AgSb is proposed. The crystal structure and electronic structure are analyzed. Furthermore, the electronic transport properties, phonon transport properties, and lattice thermal conductivity are studied using density functional theory (DFT) and the Boltzmann transport equation. The isotropic thermoelectric performance is evaluated. The analysis of strong phonon anharmonicity explains the low thermal conductivity, and the exploration of crystal symmetry uncovers the promotion of symmetry for phonon scattering. The present results provide a high-quality thermoelectric material, which will promote the theoretical and experimental research of FH materials.

II. CALCULATION METHODS

All the calculations are performed with the Vienna *ab initio* simulation package (VASP) [18] based on DFT. The cutoff energy for the plane-wave expansion is set to be 600 eV. The Perdew-Burke-Ernzerhof (PBE) [19] pseudopotentials [20] with valence electrons $5s^25p^66s^2$, $4d^{10}5s^1$, and $5s^25p^3$ are adopted for Ba, Ag, and Sb, respectively. The energy convergence criterion of the electron self-consistency is set to 10^{-7} eV/Å, and the Hellmann-Feynman force is less than 0.001 eV/Å for structure optimization. A Monkhorst-Pack $11 \times 11 \times 11$ **k**-mesh is used for structure optimizations. The hybrid function of Heyd-Scuseria-Ernzerhof (HSE06) [21] is used to estimate the electronic band structure. The Boltzmann transport equation within the rigid band and relaxation time approximations in the BoltzTraP program [22] is used to calculate σ and S. The Wiedemann-Franz law ($\kappa_e = L\sigma T$) is used to calculate κ_e [7,23]. The harmonic second-order force constants are calculated using the density functional perturbation theory (DFPT) method [24] with $2 \times 2 \times 2$ supercell and $3 \times 3 \times 3$ **k**-mesh. The phonon dispersion curve is calculated in Phonopy [25]. The phonon transport properties are evaluated using the Boltzmann transport equation with the second-order and third-order interaction force constants as implemented in the ShengBTE code [26].

The carrier lifetimes τ are calculated from the electron-phonon (e-ph) scattering rates around the valence band maximum (VBM) and conduction band minimum (CBM), as implemented in the QUANTUM ESPRESSO (QE) package [27,28]. The first-principles DFT calculations for the Wannier-Fourier interpolations are carried out within a uniform **k**-point mesh of $8 \times 8 \times 8$. The dynamic matrices are calculated with a **q**-point mesh of $2 \times 2 \times 2$. In the calculations of Electron-Phonon coupling using Wannier function (EPW), 32 Wannier functions are used to describe the conduction band and valence band, and the interpolated **k/q**-point mesh of $40 \times 40 \times 40$ is applied to solve the electron-phonon matrix elements $g_{mn,v}(\mathbf{k},\mathbf{q})$ [29].

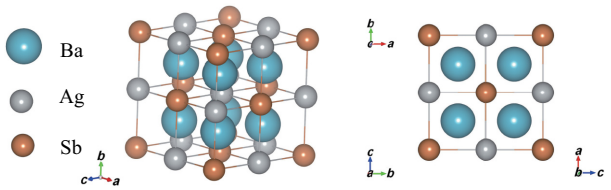

FIG. 1. The crystal structure of Ba_2AgSb. The blue, gray, and brown spheres represent the Ba, Ag, and Sb atoms, respectively.

III. RESULTS AND ANALYSES

A. Structural properties

The Ba_2AgSb compound has an average NaCl structure with the $Fm\bar{3}m$ space group, as demonstrated in Fig. 1. Sb locates at the Na (4*a*) site, Ag takes up the Cl (4*b*) site, and Ba occupies the 8*c* site. The optimized lattice constant is 5.935 Å. The bond lengths of Ba–Ag/Sb and Ag–Sb are 3.634 and 4.197 Å, respectively. Based on the optimized structure, the electronic band structure is calculated using the PBE [19] function with the HSE06 hybrid function [21]. The electronic band structure of the first Brillouin zone is shown in Fig. 2. Ba_2AgSb is a semiconductor with an indirect band gap of 0.49 eV (HSE06). It is obvious that the VBM locates between Γ and L points and the CBM lies between Γ and X points. The degeneracy of the electronic band at the Γ point has an important impact on electronic transport properties [3]. The charge carrier pockets and electronic band degeneracy near the Fermi level create additional conducting pathways, which will result in low electrical resistivity. The bottom conduction band is not degenerate, and mainly composed of Ba p orbital and contains no obvious contribution from Ag and Sb atoms, as shown in Fig. 2. Therefore, it is expected that n doping on Ag and Sb sites minimally affects the CBM, which provides specific areas for alloying and doping but maintains stable p carrier mobility. Alloying on Ag and Sb sites will enhance phonon scattering and reduce thermal conductivity. Ag (s) and Sb (p) contribute to the upper valence band, determining the features of the upper valence band edge.

The electron localization function (ELF) [30] is calculated to analyze the atomic bonds. The 3D ELF is shown in Fig. 3. The local charges around Ba and Ag are $5s^25p^6$ and $4d^{10}$ electrons, as shown in Fig. 3(a). The ELF = 0.2 surrounds all the atoms, suggesting the existence of metallic bonds, as demonstrated in Fig. 3(b); thus Ba_2AgSb is a metallic compound. Furthermore, Bader charge analysis

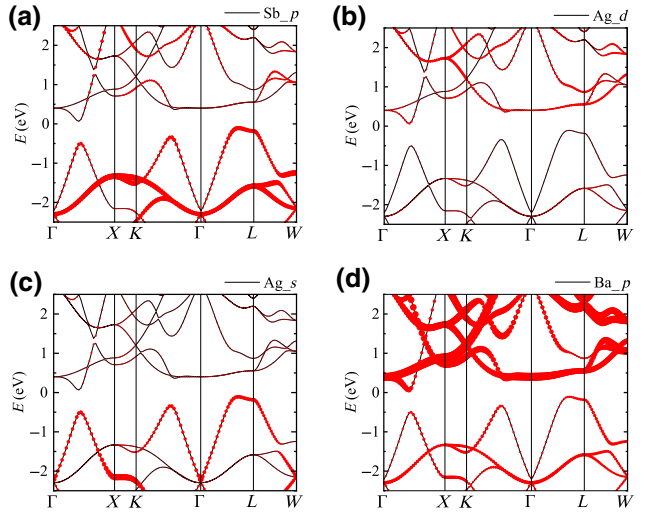

FIG. 2. The partial electronic band structure (PBE) of Sb *s* (a), Ag *d* (b), Ag *s* (c), and Ba *p* (d).

[31] is conducted to evaluate the valence charge exchange. Each Ba contributes approximately one electron to AgSb because of the large electronegativity of AgSb.

According to the electronic density of states (DOS), the electronic transport properties are predicted. The evolutions of S, σ, and κ_e with carrier concentration at 300, 500, and 800 K are displayed in Fig. 4. The electronic transport properties are isotropic for the invisible difference of S, σ, and κ_e from all directions. The value of S grows with an increase of temperature, while κ_e increases as more electrons are excited to participate in thermal transportation. Since *p*-type Ba_2AgSb has higher S than the *n*-type system, Ba_2AgSb exhibits a greater *p*-type Seebeck effect. The room-temperature S of *n*-type Ba_2AgSb is $323.6\mu\,V\,K^{-1}$ when the carrier concentration is approximately 8.37×10^{18} cm^{-3}. This is comparable to that of Ca_2YZ [17]. The higher *n*-type electrical conductivity than *p*-type shows high electronic thermal conductivity, which is harmful to thermoelectric performance. The electrical conductivity of *n*-type Ba_2AgSb is 2271.7 $S\,cm^{-1}$ at room temperature, which is much higher than that of the well-known compound $AgPb_{10}SbTe_{12}$ [32], whose room-temperature

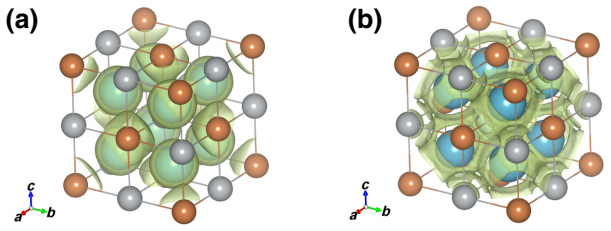

FIG. 3. The 3D ELF. The ELF value of the isosurface is 0.5 (a) and 0.2 (b).

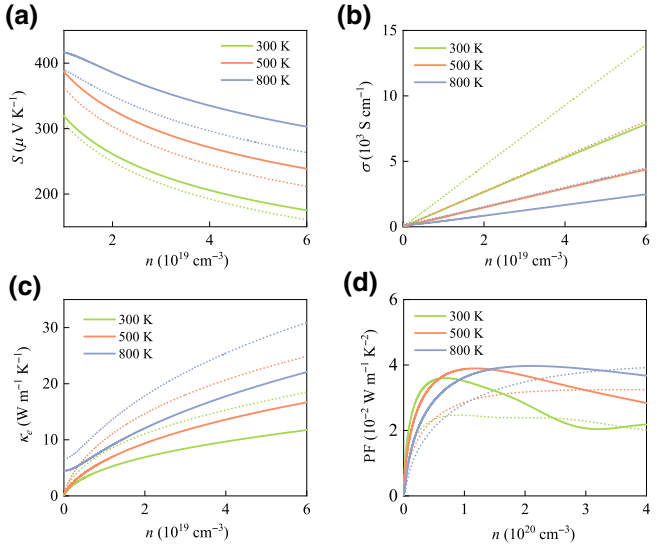

FIG. 4. The evolution of electronic transport properties with carrier concentrations n. (a) Seebeck coefficient S, (b) electrical conductivity σ, (c) electronic thermal conductivity κ_e, and (d) thermoelectric power factor (PF). The solid and dashed lines represent the properties of *n*-type and *p*-type Ba_2AgSb, respectively. The green, orange, and blue lines represent the properties at 300, 500, and 800 K, respectively.

electrical conductivity is over 520 $S\,cm^{-1}$ [32]. The thermoelectric power factor ($PF = S^2\sigma$) as a function of carrier concentration is plotted in Fig. 4(d). It is clear that *n*-type Ba_2AgSb exhibits a significantly higher PF value than the *p*-type system. The optimal PF value is much higher than that of well-known thermoelectric materials, such as LaCuOSe [33] and Sr_2BiAu [34].

B. Phonon transport properties

The flat phonon dispersion curves and phonon DOS are shown in Fig. 5. The real frequency vibrations demonstrate the dynamic stability of Ba_2AgSb. The acoustic modes are highlighted for they are mainly responsible for thermal transport [35]. For phonons obeying the Bose-Einstein statistical distribution, the increase of frequency decreases the phonon numbers, and this makes the phonons concentrate in the low-frequency region. Hence, the phonon-phonon scattering is intense in the low-frequency region. The dotted line at 1.5 THz in the phonon DOS is a reference because the vibrations below 1.5 THz are mainly responsible for thermal transport. Low-frequency vibrations of atoms indicate the loose atomic bonding in Ba_2AgSb, which is consistent with the above analysis. The high-frequency optical vibrations are mainly produced by Ba and Sb. The acoustic branches are mainly contributed by Ba and Ag, and the contribution of Ag is more obvious at 1.5 THz. Atomic vibrations are different from those of BaAgSb in $P6_3/mmc$ symmetry, in which Ag and

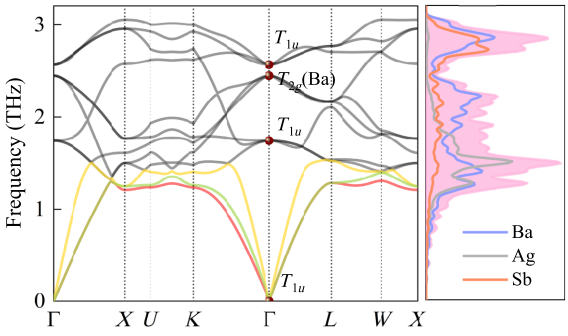

FIG. 5. The phonon dispersion curves and partial phonon density of states.

Sb vibrate with high frequency, and this emphasizes the impact of atomic arrangement on the thermal transport. The acoustic branches and soft optical branches are coupled with each other. A large amount of phonons in the crossing region indicates the strong interactions between acoustic and optical branches [33], which results in strong phonon scattering, thus low thermal conductivity. The phonon in the crossing region is mainly contributed by Ba and Ag, indicating that the contribution of Ag and Ba to the phonon scattering comes from the acoustic-optical interaction. The low-frequency acoustic phonon is mainly contributed by Ba and Ag, which demonstrates that Ba and Ag play an essential role in suppressing the lattice thermal conductivity. The optical phonon is highly degenerate at the Γ point. The lowest optical frequency is 41.71 cm^{-1}, comparable to that of SnSe (approximately 50 cm^{-1}) [36], suggesting severe optical branch softening. The highest frequencies of the three acoustic branches are 51.39, 46.71, and 43.71 cm^{-1}, respectively, which are lower than that of $AgSnSbSe_3$ (60 cm^{-1}) [10].

The phonon velocity describes the phonon transportability, which is proportional to lattice thermal conductivity. The flat acoustic modes give rise to small group velocities, which lead to lower lattice thermal conductivity, as demonstrated in Fig. 6(a). The group velocities of acoustic modes are colored as they mainly contribute to thermal transport. The LA mode possesses the highest sound velocity (3.2 km s^{-1}) in the first Brillouin zone, consistent with the highest frequency of the LA mode. The average acoustic sound velocity is 1.89 km s^{-1}, which is smaller than that of $AgSbSbSe_3$ (2.1 km s^{-1}) [10].

The acoustic sound velocities in **k**-space are shown in Fig. 6(b). The average sound velocity of acoustic branches at the Γ point is approximately 2.7 km s^{-1}, which is lower than that of bulk and monolayer phosphorene [11]. The three-phonon scattering phase space (P) is another parameter to describe the phonon-phonon scattering property. The room-temperature P is plotted in Fig. 6(c). The acoustic P is much higher than the optical P, which is consistent

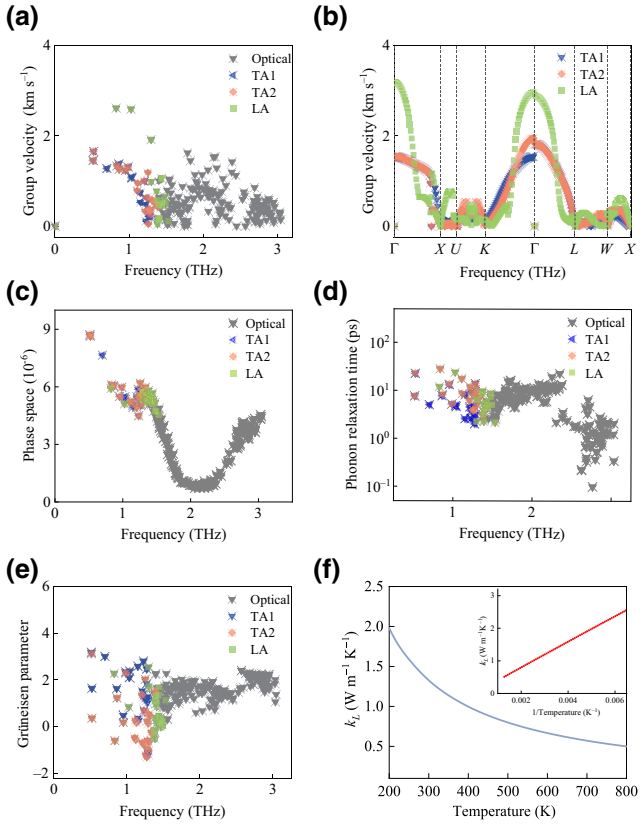

FIG. 6. The group velocities (a) and the acoustic sound velocities in **k**-space (b). The three-phonon scattering phase space (c), phonon relaxation time (d), Grüneisen parameter (e), and evolution of lattice thermal conductivity (f). The blue, orange, and green points represent the contribution of TA1, TA2, and LA phonon branches and the purple dot represents the participation of optical phonon.

with the dominant state of acoustic phonon for the lattice thermal conductivity.

The phonon relaxation time is calculated to describe the intensity of phonon-phonon scattering in Ba_2AgSb. The small phonon relaxation time demonstrates intense phonon scattering. A great amount of phonon in the cross region also contributes to the strong phonon scattering in Ba_2AgSb. To evaluate the anharmonicity, the Grüneisen parameter is calculated, as shown in Fig. 6(e). Large Grüneisen parameters mainly occur in the low-frequency region, indicating the strong anharmonicity of the acoustic phonon. The negative value of the Grüneisen parameter suggests the existence of negative thermal expansion. The average room-temperature Grüneisen parameter (1.44) is close to that of α-MgAgSb (1.5) [37], which emphasizes the strong anharmonicity of Ba_2AgSb.

Following previous research, materials with large Grüenisen parameters and loose atomic bonds have low thermal conductivity [38], which is consistent with the

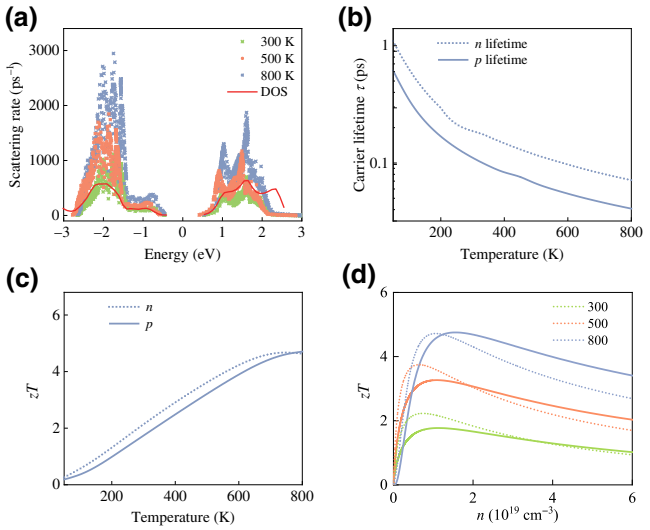

FIG. 7. (a) The electron-phonon scattering rates $1/\tau$ at 300, 500, and 800 K. (b) The temperature-dependent carrier lifetime around the VBM and CBM. The evolution of zT with (c) temperature and (d) carrier concentration. The dashed lines represent the properties of n-type Ba_2AgSb and the solid lines represent the properties of p-type Ba_2AgSb.

results for Ba_2AgSb. The thermal conductivities in consideration of the three-phonon scattering process are calculated. Four-phonon scattering is neglected because of its weak impact on the phonon transport in materials without optical-acoustical gaps [39]. The lattice thermal conductivities κ_L are the same in each direction, indicating the isotropic thermal transport ability of Ba_2AgSb. κ_L is linear with inverse temperature, as shown in Fig. 6(f), matching with the consideration of phonon Umklapp scattering. The acoustic branches dominate the thermal transport as they provide a large thermal weight factor and more phonons than optical branches. The thermal conductivity decreases with increasing temperature because more phonons are excited at high temperature. The intrinsic lattice thermal conductivity is 1.33 $W\,m^{-1}\,K^{-1}$ at 300 K, and it decreases to 0.5 $W\,m^{-1}\,K^{-1}$ at 800 K, which is lower than that of hexagonal BaAgSb [40] and comparable to that of ultralow-lattice-thermal-conductivity materials Ca_2YZ (0.85–1.6 $W\,m^{-1}\,K^{-1}$) [17].

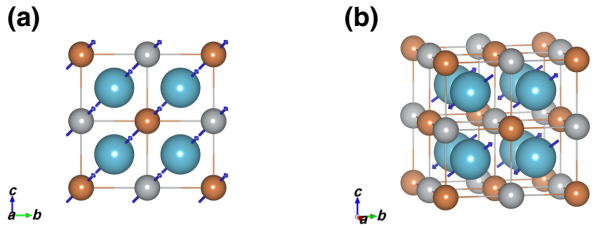

FIG. 8. Schematic representation of selected phonon modes: T_{1u} (a) and T_{2g} (b).

C. Figure of merit

During the calculation of thermoelectric performance, τ is the input parameter in Boltzmann transport equations. τ is calculated according to the imaginary part of electron self-energy. The electron and hole lifetime is calculated in the EPW model, as shown in Fig. 7(a). The e-ph scattering is intense at high temperatures, corresponding to the shorter lifetime (approximately 10^{-14} s at 800 K). According to the e-ph calculations, the room-temperature carrier lifetime near the VBM and CBM is around 1.10×10^{-13} and 1.32×10^{-13} s. The evolution of maximum zT with temperature is shown in Fig. 7(c). The n-type Ba_2AgSb shows better performance than the p-type system, more clearly at low temperatures. The room-temperature zT is 2.14. The n-type Ba_2AgSb has maximum zT of 4.7 at 750 K, which is comparable to that of gold-based FH thermoelectric materials [34,41]. The efficiency of thermoelectric performance increases with carrier concentration and reaches an optimal value, as shown in Fig. 7(d). zT reaches a maximum value when the doping concentration of electrons is around 1.57×10^{19} cm^{-3}.

D. Symmetry analysis of phonons

The symmetry of phonons in fcc Ba_2AgSb is analyzed using the irreducible representation of space groups [42]. Ba_2AgSb belongs to the space group of O_h, with Ba, Ag, and Sb occupying 8c, 4b, and 4a sites with symmetry of Td (Ba) and Oh. The high-symmetry points Γ, X, W, and L in the first Brillouin zone have symmetry of O_h, D_{4h}, D_{2v}, and C_{3v}, respectively. The IR-active modes are all acoustic modes with the irreducible representation of T_{1u} [42]. The Raman-active mode is T_{2g} and is contributed by Ba. According to the irreducible representations, the vibration directions of each representation are shown in Fig. 8. All the phonon branches have three-fold degeneracy at the Γ point. According to the phonon dispersion curves, the Debye frequency is 3 THz at the X point, and

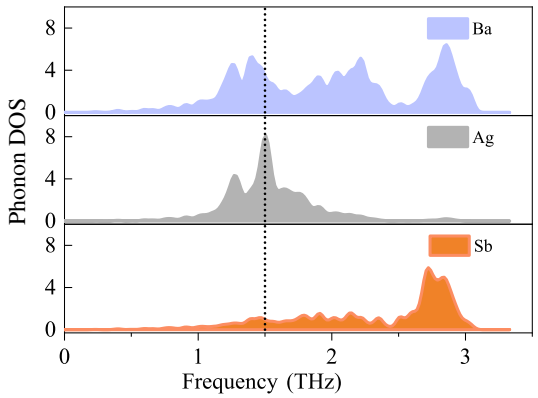

FIG. 9. Partial phonon DOS.

TABLE I. The three-phonon scattering channels along the high-symmetry paths.

High-symmetry path	$\Gamma \to K/U\,(C_{2v})$	$\Gamma \to L\,(C_{3v})$	$\Gamma \to X\,(D_{4h})$	$\Gamma \to W\,(D_{2d})$
Irreducible representation	$T_{2g} \to A_2 + B_1 + B_2$ $T_{1u} \to A_1 + B_1 + B_2$	$T_{2g} \to A_1 + E$ $T_{1u} \to A_1 + E$	$T_{2g} \to B_{2g} + E_g$ $T_{1u} \to A_{2u} + E_u$	$T_{2g} \to B_2 + E$ $T_{1u} \to B_2 + E$
Three-phonon scattering channels	$A_1\ A_1\ A_1$ $A_1\ A_2\ A_2$ $A_1\ B_1\ B_1$ $A_1\ B_2\ B_2$ $A_2\ B_1\ B_2$	$A_1\ A_1\ A_1$ $A_1\ E\ E$ $E\ E\ E$	$A_{2u}\ E_u\ E_g$ $B_{2g}\ E_u\ E_u$ $B_{2g}\ E_g\ E_g$	$B_2\ E\ E$

the corresponding $|X|$ is q_D. The energy and momentum criteria of phonon Umklapp scattering are: $\hbar\omega_1 + \hbar\omega_2 = \hbar\omega_3$ and $\vec{k}_1 + \vec{k}_2 = \vec{k}_3 + \vec{G}$.

Phonon Umklapp scattering redistributes phonon momentum spectra. Phonon around $1/2\ q_D$ dominates the phonon Umklapp scattering. There, q_D is $0.79|\mathbf{b}|$, where $\mathbf{b}$ is the reciprocal lattice vector. The phonon in the region of $|\mathbf{q}| < 1/2\,q_D$ is almost the low-frequency (< 1 THz) acoustic phonon, which accounts for the small P, high group velocity, and small Grüneisen parameter in this region. Ag makes a significant contribution in the low-frequency region, and this is more obvious below 1.5 THz, as demonstrated in Fig. 9. The symmetry operations of Ba_2AgSb are 48. Both atomic composition and crystal symmetry affect the thermal conductivity to some extent. The effect of the composition cannot be studied due to the limitations of first-principles calculations, but the effect of symmetry is still discussed. The crystal symmetry restricts the phonon-phonon scattering selection rules [13]. According to the three-phonon scattering rules [12], the scattering channels at Γ points along the high-symmetry paths are listed in Table I. All of the high-symmetry paths have three-phonon scattering channels, indicating the favorability of symmetry-based phonon scattering. So, this framework can be used to insert different elements to optimize the thermoelectric properties during high-throughput calculations. The phonon representations of Ba_2AgSb at the high-symmetry point in the first Brillouin zone are defined as: $\Gamma := \Gamma_{\text{ac}} + \Gamma_{\text{opt}} = 3\Gamma_4^- + \Gamma_5^+ = 3T_{1u} + T_{2g}, \Gamma_{\text{ac}} = \Gamma_4^- = T_{1u}, \Gamma_{\text{opt}} = 2\Gamma_4^- + \Gamma_5^+ = 2T_{1u} + T_{2g}$. According to crystal symmetry, the breakdown of the symmetry along the high-symmetry path is analyzed. The triply degenerate T_{1u} and T_{2g} symmetry at the Γ point breaks down to A_1 and E symmetry at the L point, but T_{1u} symmetry breaks down to A_{2u} and E_u symmetry, and T_{2g} breaks down to B_{2g} and E_g symmetry at the X point. In addition, all the triply degenerate phonon branches break down to B_2 and E on the Γ-W path. The symmetry breakdown along Γ-K (L/X) paths splits triply degenerate modes into one doubly degenerate mode and one nondegenerate mode. Furthermore, all the phonon branches are nondegenerate at U and K points, which introduce a variety of phonon-phonon scattering paths and restrain the thermal transport.

IV. CONCLUSIONS

Using our first-principles calculations, the thermoelectric performance of Ba_2AgSb is investigated. Ba_2AgSb is a promising isotropic thermoelectric material with intense phonon-phonon scattering and strong phonon anharmonicity, which induces low intrinsic lattice thermal conductivity (κ_L). The lattice thermal conductivity is 1.33 $\text{W m}^{-1}\text{K}^{-1}$ at 300 K and drops to 0.5 $\text{W m}^{-1}\text{K}^{-1}$ at 800 K. Ba_2AgSb has a maximum zT of 4.7 at 750 K with electron doping concentration of about 1.57×10^{19} cm^{-3}. The analysis of partial phonon density indicates that Ba and Ag inhibit thermal transport by the acoustic-optic phonon coupling. Ag has a significant influence on thermal transport, mainly on phonon Umklapp scattering. The symmetry-based phonon scattering rules are listed, and a high-quality crystal framework for high-throughput screening is given. As a result, low-cost FH compound Ba_2AgSb with high thermoelectric performance is considered to have potential thermoelectric applications.

ACKNOWLEDGMENTS

The calculations were performed at the Supercomputer Centre in the China Spallation Neutron Source, and we thank the workers in the Supercomputer Centre. This work is supported by the Science Center of the National Natural Science Foundation of China (Grant No. 52088101), the National Natural Science Foundation of China (Grants No. 11675195, No. U1932220, and No. 12074381), the National Key R&D Program of China (Grant No. 2017YFA0403700), the Key Research Program of Frontier Sciences, CAS (Grant No. 292016YQYKXJ00135), and the Guangdong Basic and Applied Basic Research Foundation (Grant No. 2019A1515111025).

APPENDIX A: ELECTRONIC BAND STRUCTURE AND PHONON DISPERSION CURVES CALCULATED IN QE

The same crystal structure is used in VASP and QE calculations. The electronic band structure and phonon dispersion curve in the first Brillouin zone are calculated in QUANTUM ESPRESSO, as shown in Fig. 10. Both electronic

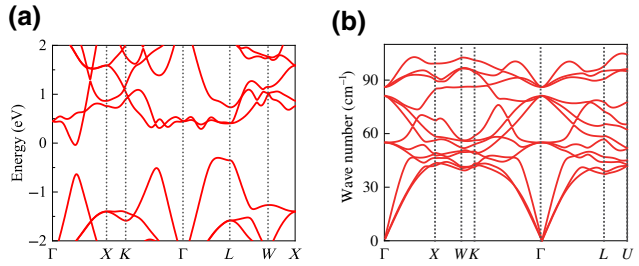

FIG. 10. The electronic band structure (a) and phonon dispersion curve (b) calculated in QE.

and phonon band structures are the same as that of VASP, implying the consistency of our DFT calculations.

APPENDIX B: THE CONVERGENCE TEST OF k/q-POINT MESHES

The scattering rates close following the electronic density of states, implying the rational EPW calculation. The convergence of **k**/**q**-point meshes is tested using $20 \times 20 \times 20$ and $25 \times 25 \times 25$ **k**/**q**-point meshes, as shown in Fig. 11(a). The ignorable difference between these two meshes confirms the convergence. The carrier lifetimes calculated by $20 \times 20 \times 20$ and $40 \times 40 \times 40$ **k**/**q**-point meshes are shown in Fig. 11(b).

APPENDIX C: THE CALCULATION OF ELECTRONIC THERMAL CONDUCTIVITY

The Wiedemann-Franz law ($\kappa_e = L\sigma T$) is used to calculate the electronic thermal conductivity [7]. The Lorentz number is calculated according to $L = 1.5 + \exp[-\text{abs}(S)/116]$ [23], as shown in Fig. 12. S is the Seebeck coefficient, which is calculated using the BoltzTraP program [22].

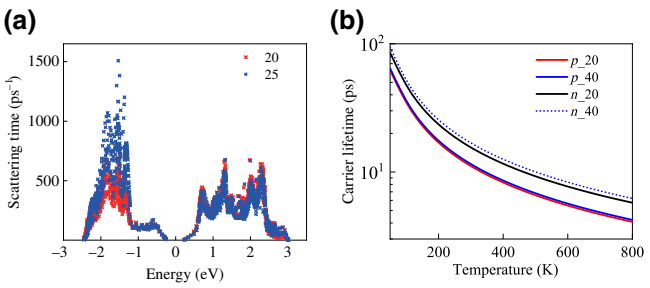

FIG. 11. (a) The carrier lifetimes calculated with $20 \times 20 \times 20$ and $25 \times 25 \times 25$ **k**/**q**-point meshes. (b) The carrier lifetimes calculated with $20 \times 20 \times 20$ and $40 \times 40 \times 40$ **k**/**q**-point meshes.

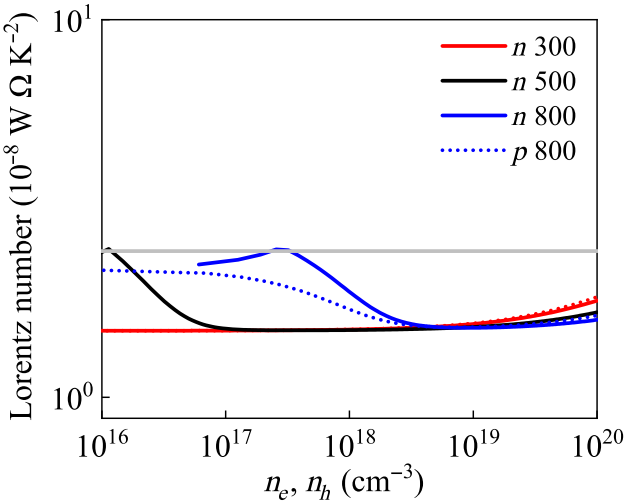

FIG. 12. The evolution of Lorentz number.

[1] S. Hao, L. Ward, Z. Luo, V. Ozolins, V. P. Dravid, M. G. Kanatzidis, and C. Wolverton, Design strategy for high-performance thermoelectric materials: The prediction of electron-doped $KZrCuSe_3$, Chem. Mater. **31**, 3018 (2019).

[2] Y. Zhao, C. Lian, S. Zeng, Z. Dai, S. Meng, and J. Ni, Anomalous electronic and thermoelectric transport properties in cubic Rb_3AuO antiperovskite, Phys. Rev. B **102**, 094314 (2020).

[3] Y. Pei, H. Wang, and G. J. Snyder, Band engineering of thermoelectric materials, Adv. Mater. **24**, 6125 (2012).

[4] L.-P. Hu, T.-J. Zhu, X.-H. Liu, and X.-B. Zhao, Point defect engineering of high-performance bismuth-telluride-based thermoelectric materials, Adv. Funct. Mater. **24**, 5211 (2014).

[5] A. Minnich, M. S. Dresselhaus, Z. Ren, and G. Chen, Bulk nanostructured thermoelectric materials: Current research and future prospects, Energy Environ. Sci. **2**, 466 (2009).

[6] G. Tan, F. Shi, H. Sun, L.-D. Zhao, C. Uher, V. P. Dravid, and M. G. Kanatzidis, SnTe–$AgBiTe_2$ as an efficient thermoelectric material with low thermal conductivity, J. Mater. Chem. A **2**, 20849 (2014).

[7] L.-D. Zhao, G. Tan, S. Hao, J. He, Y. Pei, H. Chi, H. Wang, S. Gong, H. Xu, and V. P. Dravid, *et al.*, Ultrahigh power factor and thermoelectric performance in hole-doped single-crystal SnSe, Science **351**, 141 (2016).

[8] Y. Zhao, Z. Dai, C. Lian, and S. Meng, Exotic thermoelectric behavior in nitrogenated holey graphene, RSC Adv. **7**, 25803 (2017).

[9] S. Zeng, Y. Zhao, G. Li, and J. Ni, Strongly enhanced superconductivity in doped monolayer MoS_2 by strain, Phys. Rev. B **94**, 024501 (2016).

[10] Y. Luo, S. Hao, S. Cai, T. J. Slade, Z. Z. Luo, V. P. Dravid, C. Wolverton, Q. Yan, and M. G. Kanatzidis, High thermoelectric performance in the new cubic semiconductor $AgSnSbSe_3$ by high-entropy engineering, J. Am. Chem. Soc. **142**, 15187 (2020).

[11] X.-L. Zhu, P.-F. Liu, J.-R. Zhang, P. Zhang, W.-X. Zhou, G.-F. Xie, and B.-T. Wang, Monolayer SnP_3: An excellent p-type thermoelectric material, Nanoscale **11**, 19923 (2019).

[12] R. Yang, S. Yue, Y. Quan, and B. Liao, Crystal symmetry based selection rules for anharmonic phonon-phonon scattering from a group theory formalism, Phys. Rev. B **103**, 184302 (2021).

[13] A. Cammarata, Phonon–phonon scattering selection rules and control: An application to nanofriction and thermal transport, RSC Adv. **9**, 37491 (2019).

[14] J. He, M. Amsler, Y. Xia, S. S. Naghavi, V. I. Hegde, S. Hao, S. Goedecker, V. Ozoliņš, and C. Wolverton, Ultralow Thermal Conductivity in Full Heusler Semiconductors, Phys. Rev. Lett. **117**, 046602 (2016).

[15] H. Yuan, C. Sheng, Z. Zhou, R. Hu, S. Han, and H. Liu, Promising thermoelectric performance of full-heusler compound Sr_2AuBi, Phys. Lett. A **404**, 127413 (2021).

[16] J. Ma, A. S. Nissimagoudar, S. Wang, and W. Li, High thermoelectric figure of merit of full-heusler, Ba_2AuX (X =As, Sb, and Bi), Phys. Status Solidi (RRL)–Rapid Res. Lett. **14**, 2000084 (2020).

[17] Y. Hu, Y. Jin, G. Zhang, and Y. Yan, Electronic structure and thermoelectric properties of full heusler compounds, Ca_2YZ (Y = Au, Hg; Z = As, Sb, Bi, Sn*and*Pb), RSC Adv. **10**, 28501 (2020).

[18] G. Kresse and J. Furthmüller, Efficient iterative schemes for ab initio total-energy calculations using a plane-wave basis set, Phys. Rev. B **54**, 11169 (1996).

[19] J. P. Perdew, K. Burke, and M. Ernzerhof, Generalized Gradient Approximation Made Simple, Phys. Rev. Lett. **77**, 3865 (1996).

[20] G. Kresse and D. Joubert, From ultrasoft pseudopotentials to the projector augmented-wave method, Phys. Rev. B **59**, 1758 (1999).

[21] J. Heyd, G. E. Scuseria, and M. Ernzerhof, Hybrid functionals based on a screened coulomb potential, J. Chem. Phys. **118**, 8207 (2003).

[22] G. K. Madsen and D. J. Singh, BoltzTraP.A code for calculating band-structure dependent quantities, Comput. Phys. Commun. **175**, 67 (2006).

[23] H.-S. Kim, Z. M. Gibbs, Y. Tang, H. Wang, and G. J. Snyder, Characterization of lorenz number with seebeck coefficient measurement, APL Mater. **3**, 041506 (2015).

[24] S. Baroni, S. De Gironcoli, A. Dal Corso, and P. Giannozzi, Phonons and related crystal properties from density-functional perturbation theory, Rev. Mod. Phys. **73**, 515 (2001).

[25] L. Chaput, A. Togo, I. Tanaka, and G. Hug, Phonon-phonon interactions in transition metals, Phys. Rev. B **84**, 094302 (2011).

[26] W. Li, J. Carrete, N. A. Katcho, and N. Mingo, ShengBTE: A solver of the boltzmann transport equation for phonons, Comput. Phys. Commun. **185**, 1747 (2014).

[27] P. Giannozzi, O. Andreussi, T. Brumme, O. Bunau, M. B. Nardelli, M. Calandra, R. Car, C. Cavazzoni, D. Ceresoli, and M. Cococcioni, *et al.*, Advanced capabilities for materials modelling with quantum ESPRESSO, J. Phys.: Condens. Matter **29**, 465901 (2017).

[28] P. Giannozzi, S. Baroni, N. Bonini, M. Calandra, R. Car, C. Cavazzoni, D. Ceresoli, G. L. Chiarotti, M. Cococcioni, I. Dabo, and *et al.*, QUANTUM ESPRESSO: A modular and open-source software project for quantum simulations of materials, J. Phys.: Condens. Matter **21**, 395502 (2009).

[29] S. Poncé, E. R. Margine, C. Verdi, and F. Giustino, EPW: Electron–phonon coupling, transport and superconducting properties using maximally localized wannier functions, Comput. Phys. Commun. **209**, 116 (2016).

[30] A. Savin, R. Nesper, S. Wengert, and T. F. Fässler, ELF: The electron localization function, Angewandte Chemie International Edition in English **36**, 1808 (1997).

[31] W. Tang, E. Sanville, and G. Henkelman, A grid-based bader analysis algorithm without lattice bias, J. Phys.: Condens. Matter **21**, 084204 (2009).

[32] K. F. Hsu, S. Loo, F. Guo, W. Chen, J. S. Dyck, C. Uher, T. Hogan, E. Polychroniadis, and M. G. Kanatzidis, Cubic $AgPb_mSbTe_{2+m}$: Bulk thermoelectric materials with high figure of merit, Science **303**, 818 (2004).

[33] N. Wang, M. Li, H. Xiao, X. Zu, and L. Qiao, Layered LaCuOSe: A Promising Anisotropic Thermoelectric Material, Phys. Rev. Appl. **13**, 024038 (2020).

[34] J. Park, Y. Xia, and V. Ozoliņš, High Thermoelectric Power Factor and Efficiency from a Highly Dispersive Band in Ba_2BiAu, Phys. Rev. Appl. **11**, 014058 (2019).

[35] P.-F. Liu, T. Bo, J.-P. Xu, W. Yin, J.-R. Zhang, F.-W. Wang, O. Eriksson, and B.-T. Wang, First-principles calculations of the ultralow thermal conductivity in two-dimensional group-IV selenides, Phys. Rev. B **98**, 235426 (2018).

[36] L.-D. Zhao, S.-H. Lo, Y.-S. Zhang, H. Sun, G.-J. Tan, C. Uher, C. Wolverton, V. P. Dravid, and M. G. Kanatzidis, Ultralow thermal conductivity and high thermoelectric figure of merit in SnSe crystals, Nature **508**, 373 (2014).

[37] X.-Y. Li, P.-F. Liu, E.-Y. Zhao, Z.-G. Zhang, T. Guidi, M. D. Le, M. Avdeev, K. Ikeda, T. Otomo, M. Kofu, and et al, Ultralow thermal conductivity from transverse acoustic phonon suppression in distorted crystalline α-MgAgSb, Nat. Commun. **11**, 1 (2020).

[38] G. A. Slack, The thermal conductivity of nonmetallic crystals, Solid State Phys. **34**, 1 (1979).

[39] N. K. Ravichandran and D. Broido, Phonon-Phonon Interactions in Strongly Bonded Solids: Selection Rules and Higher-Order Processes, Phys. Rev. X **10**, 021063 (2020).

[40] S.-F. Wang, Z.-G. Zhang, B.-T. Wang, J.-R. Zhang, and F.-W. Wang, Zintl phase BaAgSb: Low thermal conductivity and high performance thermoelectric material in ab initio calculation, Chin. Phys. Lett. **38**, 46301 (2021).

[41] J. Park, Y. Xia, A. M. Ganose, A. Jain, and V. Ozoliņš, High Thermoelectric Performance and Defect Energetics of Multipocketed Full Heusler Compounds, Phys. Rev. Appl. **14**, 024064 (2020).

[42] M. I. Aroyo, J. Perez-Mato, D. Orobengoa, E. Tasci, G. de la Flor, and A. Kirov, Crystallography online: Bilbao crystallographic server, Bulg. Chem. Commun. **43**, 183 (2011).